Title
Understanding Surface Densified Phases in Ni-Rich Layered Compounds

Journal
ACS Energy Letters, 4(4)

ISSN
2380-8195

Authors
Xiao, Penghao
Shi, Tan
Huang, Wenxuan
et al.

Publication Date
2019-04-12

DOI
10.1021/acsenergylett.9b00122

Peer reviewed

ACS Energy LETTERS

Cite This: ACS Energy Lett. 2019, 4, 811−818

http://pubs.acs.org/journal/aelccp

LETTER

Understanding Surface Densified Phases in Ni-Rich Layered Compounds

Penghao Xiao,[†,§] Tan Shi,[‡] Wenxuan Huang,[¶] and Gerbrand Ceder*[,‡]

[†]Materials Sciences Division, Lawrence Berkeley National Laboratory, Berkeley, California 94720, United States

[‡]Department of Materials Science and Engineering, University of California, Berkeley, California 94720, United States

[¶]Department of Materials Science and Engineering, Massachusetts Institute of Technology, Cambridge, Massachusetts 02139, United States

Supporting Information

ABSTRACT: Understanding structural transformation at the surface of Ni-rich layered compounds is of particular importance for improving the performance of these cathode materials. In this Letter, we identify the surface phases using first-principles-based kinetic Monte Carlo simulations. We show that slow kinetics precludes the conventional $Li_{0.5}NiO_2$ spinel to form from its layered parent phase at room temperature. Instead, we suggest that densified phases of the types $Ni_{0.25}NiO_2$ and $Ni_{0.5}NiO_2$ can form by Ni back diffusion from the surface owing to oxygen loss at highly charged states. Our conclusion is supported by the good agreement between the simulated STEM images and diffraction patterns and previously reported experimental data. While these phases can be mistaken for spinel and rock salt structures in STEM, they are noticeably different from these common structure types. We believe that these results clarify a long-standing puzzle about the nature of surface phases on this important class of battery materials.

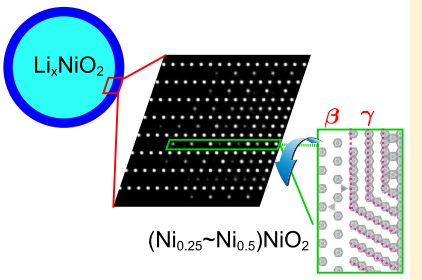

An efficient energy storage solution is the key component for a clean energy future. Li-ion batteries have shown their advantage in many applications from small electronic devices to electric vehicles. One limiting factor for Li-ion batteries to reach higher energy and power densities is the cathode material. Ni-rich layered compounds, including NMC ($LiNi_xMn_yCo_{1-x-y}O_2$) and NCA ($LiNi_{0.8}Co_{0.15}Al_{0.05}O_2$), have among the highest energy densities of commercialized cathode materials. One important degradation mechanism of these materials is the formation of densified phases near the particle surface, which are believed to be the cause of increased impedance and lowered rate capability.[1−10] Identifying this new surface phase and understanding its formation mechanism are important for improving the long-term performance of these materials. A spinel-like phase has often been observed near the particle surface by scanning transmission electron microscopy (STEM) studies, with sometimes a rock-salt-like phase present at the very surface.[9,11−13] Experimental thermal stability studies and computed phase diagrams indicate that the spinel phase is thermodynamically stable at the $Li_{0.5}NiO_2$ composition with a significant driving force to form from the layered phase (51 meV per oxygen).[14−20] The formation of spinel $Li_{0.5}NiO_2$ after cycling seems therefore well justified from the thermodynamic point of view. However, experimentally the spinel-like phase does not form throughout the particle but only near the surface, which suggests that either kinetic hurdles prevent the transformation in the bulk region or the surface spinel-like phase is different in nature. Moreover, it has been reported that the densified phase in NCA has diffraction patterns forbidden by the spinel symmetry.[12] The exact nature of the new phase therefore remains controversial.

Because these surface phases may control Li transport into the cathode, it is important to establish in more detail what their structure and composition are as the diffusivity through partially disordered phases can depend critically on the Li to metal ratio[21] as well as the nature of the local order around the sites that make up the Li migration path.[22,23] STEM and electron diffraction (ED) data on the surface phases are often modeled with common well-known phases, such as "spinel" and "rock salt". We show in this Letter through ab initio kinetic modeling of the densification process that this "rock salt + spinel" picture may be oversimplified and that other phases are likely present near the surface.

One special aspect about the surfaces of layered cathodes is that oxygen loss occurs during the initial charges, leaving excess transition metal behind. Back diffusion of the transition metal leads to the formation of the densified surface phases.[12,24−27] The phase diagram, as calculated from first-principles, predicts the existence of three Ni-excess phases, Ni_xNiO_2 with x = 0.25, 0.5, and 0.75.[19] Here x indicates Ni occupation in the Li layer. These three phases, namely, β, γ,

Received: January 16, 2019
Accepted: February 25, 2019
Published: February 25, 2019

DOI: 10.1021/acsenergylett.9b00122
ACS Energy Lett. 2019, 4, 811−818

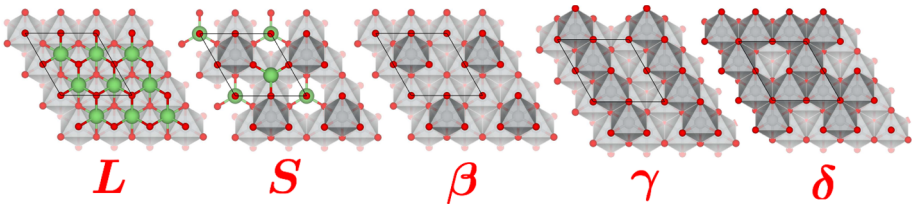

Figure 1. Five phases discussed in this Letter viewed from the top of the layers. Two adjacent layers in the structures are shown. L and S represent the layered and spinel phases, respectively. Gray octahedra are Ni; green spheres are Li; red spheres are O.

and δ as shown in Figure 1, expand the candidate pool of possible surface phases. However, thermodynamic arguments alone cannot determine which is the most likely surface phase among the four candidates, including the conventional spinel. In this study density functional theory (DFT)-based kinetic Monte Carlo (KMC) simulations are employed to study the kinetics of Ni back diffusion and phase formation. We use the cluster expansion technique to parametrize the energy of the system with respect to Ni, Li, and vacancy occupations on the octahedral and tetrahedral sites of the underlying rock salt lattice. Similar techniques have previously been used to study Li-vacancy ordering,[28−32] transition metal ordering,[33−35] and Na-vacancy ordering[36−38] in cathode materials. The values of the effective cluster interactions are extracted from DFT calculations performed with the GGA+U approach (see the Computational Methods section). KMC is then used to simulate structure evolution on experimental time scales. Because in both Ni-rich NMC and NCA the Ni percentages in transition metal layers are as high as 80%, we use layered $LiNiO_2$ as a simplified, yet representative model system. The fundamental questions to answer are what is the spinel-like phase and why is the spinel-like phase observed only near the surface.

In the rock salt lattice, every octahedral site is face-sharing with eight tetrahedral sites, and every tetrahedral sites is face-sharing with four octahedral sites. Therefore, Li-vacancy and Ni-vacancy hops between neighboring octahedral and tetrahedral sites, both parallel and perpendicular to the layered direction, are allowed in KMC. Thus, starting from the layered phase, the system can evolve to any phase that is accommodated by the rock salt lattice if energetically accessible. At each KMC step, the time increment is randomly chosen following first-order kinetics based on the total rate of all of the possible hops, and one hop is randomly selected based on its rate portion in the total rate following the approach by Bortz, Kalos, and Lebowitz.[39] The individual hopping rate is calculated from the Arrhenius equation with a constant prefactor and a barrier proportional to the energy change after the hop.

In the following paragraphs, we first show how the Ni densified phases form by Ni back diffusion from the surface. STEM images of the resulting phases are simulated to directly compare with experimental observations. We then discuss why no spinel phase is observed in the bulk regions of the Ni-rich layered materials. We show that, although the spinel structure is the ground state near the half-lithiated state, the layered structure is preserved in the bulk region due to the slow kinetics associated with this phase transition.

Phases Formed by Ni Back Diffusion. Ni densification occurs at the particle surface due to oxygen loss when the cathode is highly charged. The excess Ni then diffuses backward, forming various phases near the surface. To simulate the Ni back diffusion process, a Ni reservoir is created in the simulation box to provide excess Ni at the surface. Figure 2 depicts the initial configuration of the supercell. Within the central red box, all of the octahedral sites are filled with Ni, forming the NiO rock salt structure, and Ni ions are constantly refilled as they diffuse outward. The Ni diffusion is examined under this driving force.

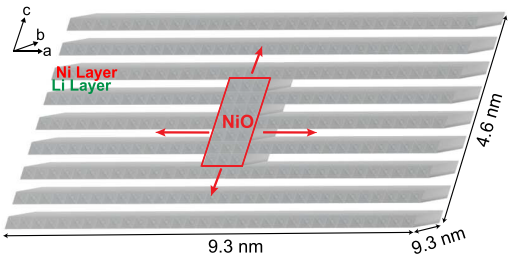

Figure 2. Model setup for simulating Ni back diffusion. Periodic boundary conditions are applied. The red box encloses the NiO reservoir where all of the octahedral sites are filled with Ni (gray) at all times. The NiO box is three sites wide along *a*, seven sites high along *c*, and periodic along *b*. Excess Ni from the NiO region will insert into the layered Li_xNiO_2 framework, growing Ni-excess surface phases along the red arrows.

Ni back diffusion was first simulated at 300 K for 11 h of physical time with 10^{10} KMC steps. The charging voltage was set at 4.8 V so that no Li was present in the material. Unlike Li, which moves only in the Li layers, Ni diffuses both along and across Li layers. Diffusion from one Li layer to the next is achieved in two steps: first a Ni atom in the transition metal layer moves to the Li layer, and then the vacancy left is filled up by another Ni nearby from the Li layer behind. To quantify the Ni back diffusion progress, an average diffusion length is calculated as $L = \frac{\sum d_i \times \sigma_i}{\sum \sigma_i}$, where d_i is the distance of site i to the NiO boundary and σ_i is the Ni occupancy of that site, and the summation is over all of the Li layer sites. d_i starts from 3 Å along a and 6 Å along c, as defined by the first sites available to the excess Ni. L can also be calculated from high-resolution STEM images from experiments. L values as a function of time, t, along both a and c directions, are plotted in Figure 3. The first observation is that Ni diffuses faster along the Li layer (along the a axis) than across layers (along the c axis). Therefore, the thickness of the Ni-excess region beneath a (001) surface should be smaller than that under a (010) surface. Densification in both directions has been observed for NCA in STEM images.[2,40] Lin et al. further showed in $LiNi_{0.4}Mn_{0.4}Co_{0.18}Ti_{0.02}O_2$ that the densified region grew thicker along the Li diffusion channels than across, consistent with our finding.[6] The second observation from Figure 3 is that the Ni insertion quickly slows down after the initial period,

DOI: 10.1021/acsenergylett.9b00122
ACS Energy Lett. 2019, 4, 811−818

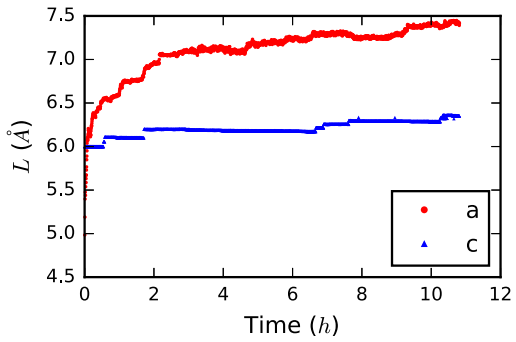

Figure 3. Average diffusion length as a function of time, $L(t)$, at 300 K.

with $\frac{dL}{dt} < 0.1$ Å/h after the first 0.5 h. This agrees with many experimental observations that densified phases are confined to a few nanometers near particle surfaces.[2,6,26,41]

STEM images of our densified structures are simulated using the Prismatic package in order to make direct comparison with experiments.[42,43] The left panel in Figure 4 is a simulated STEM image from the [010] zone axis. Excess Ni in the Li layer can be seen beyond the red box in both the *a* and *c* directions. The Ni occupation pattern is not completely random: an alternating bright/dark ordering is present along the *a* axis at the edge of the Ni-excess region, a few sites away from the red box. A spot in the STEM image represents an average occupancy of Ni in a column, but atomistic details in each column are missing. The distribution of excess Ni can be better seen in the right panel in Figure 4, which shows the top view of the single Li layer indicated by the solid green arrow. The rows of octahedral sites are aligned with their projected STEM spots on the left, as guided by the dashed black line. Although small domains of Ni-vacancy ordered phases are clearly present in the layer, its STEM column projection shows little sign of ordering. The γ phase with 50% excess Ni in the Li layer per formula unit appears near the Ni source; the β phase with 25% excess Ni in the Li layer appears far away from the Ni source. The γ phase has alternating Ni/vacancy lines that can be along any of three directions within the layer: the *a* axis, the *b* axis, or their angle bisector. The long-range ordering near the Ni source is difficult to recognize from the projection because of various orientations of the small γ phase domains. In contrast, the β phase has only one projection pattern along the above three directions and thus always shows a clear bright/dark ordering in STEM. The other Li layers have similar patterns.

The kinetics in our 300 K simulation is clearly very slow, leading to back diffusion only a few layers deep and very small ordered domains of excess Ni. Simulating beyond the 11 h of physical time is computationally extremely expensive. To get a better perspective on what may occur at longer times, we accelerated the kinetics by performing a simulation at 1000 K. In this case, the total physical time elapsed was much shorter owing to faster elemental hops at the elevated temperature, but the overall densification process was more advanced than that for the 300 K case. Figure 5a,b presents two snapshots of the 1000 K simulation at 11 and 267 μs, respectively, showing the time evolution of the Ni densified phases. The top views, on the right of this figure, indicate that the γ phase nucleated with different orientations on each side of the interface, and the β phase is present further from the interface. In Figure 5a, at 11 μs, the γ phase below the NiO region has two orientations, shown by the dashed magenta lines. In Figure 5b, after 267 μs, the two orientations of γ have merged into one. Comparing the top views in Figure 5a,b, it can be observed that the γ phase grows significantly larger with time. At 267 μs, the γ phase has the largest coverage with a maximum of eight atomic layers on both sides of the Ni source. The β phase forms further into the material with four to five layers of coverage. The δ phase with 0.75 excess Ni exists immediately next to the Ni source but is limited to two atomic layers thickness. The dominant phases formed by surface Ni back diffusion are the γ and β phases until the γ phase fills the entire supercell, after which the δ phase starts to grow further.

The orientation variance of the γ phase results in different STEM patterns, as emphasized by the two ellipses. In Figure 5a, an alternating bright/dark STEM pattern forms near the Ni source because part of the γ phase domain has alternating Ni/vacancy lines parallel to the projection direction (indicated by the dashed black lines). In contrast, in Figure 5b, this alternating bright/dark pattern disappears near the Ni source because the γ phase's Ni/vacancy lines alternate along the *a* axis. The ordering pattern from the β phase far from the Ni source remains the same for both cases. Hence, while β gives a consistent STEM projection, the γ phase can project either as alternating bright/dark spots or as a set of equivalent spots, depending on its orientation with respect to the beam.

Figure 5b makes it clear that two types of STEM patterns should be observed in the Li layer: (1) continuous spots of similar intensities that are dimmer than those in the transition metal layer, as in the green ellipse near the Ni source, or (2) an alternation of bright/dark spots. The uniformly dimmer spots in the Li layer have been reported many times in NCA and

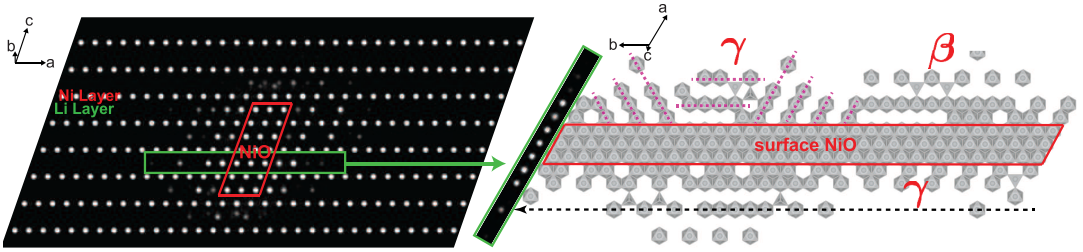

Figure 4. Left: Simulated STEM image along the [010] zone axis after holding the Li voltage at 4.8 V for 11 h at 300 K. Bright spots are Ni columns. Right: Top view of the Ni distribution in the Li layer indicated by the arrow, where gray octahedra are NiO_6 and gray spheres inside are Ni atoms. The dashed line indicates the column projection direction in STEM. The ordered $Ni_{0.5}NiO_2$ γ phase and the $Ni_{0.25}NiO_2$ β phase domains are labeled by red Greek letters. All three different orientations of the γ phase are observed, as indicated by the dashed magenta lines.

DOI: 10.1021/acsenergylett.9b00122
ACS Energy Lett. 2019, 4, 811−818

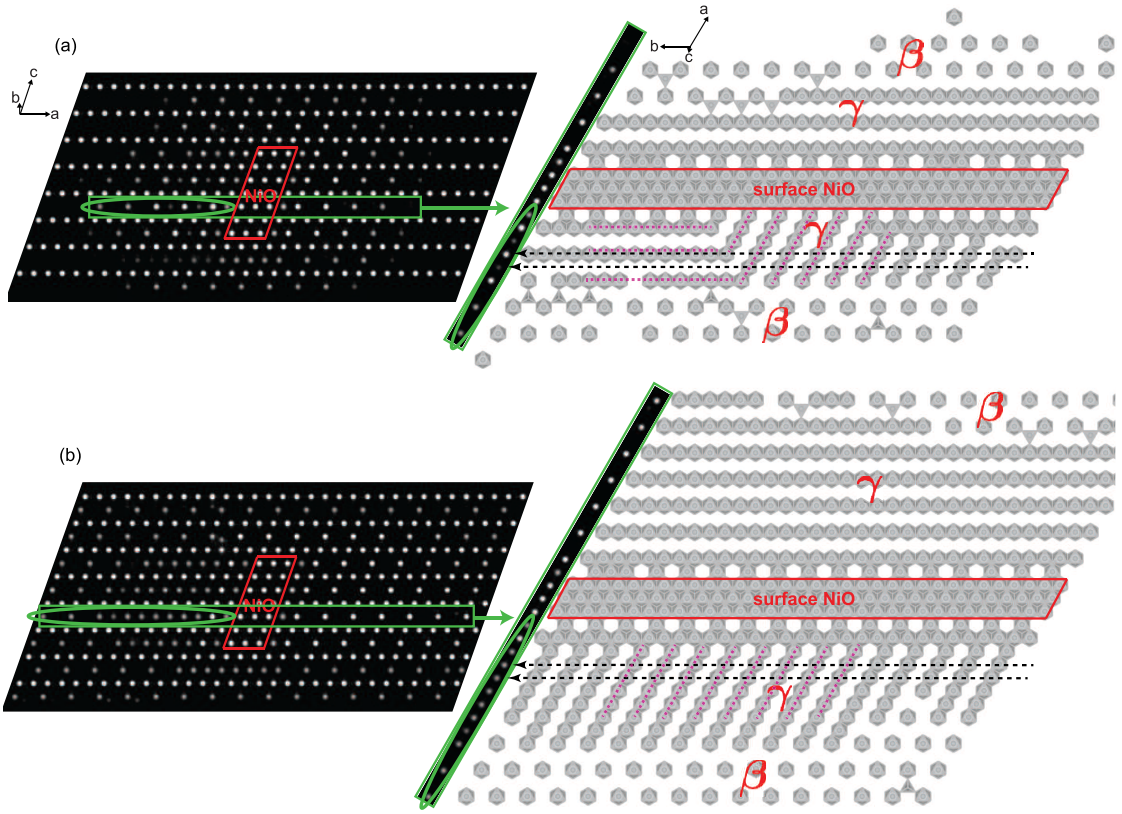

Figure 5. Simulated STEM images and top views of Ni in the Li layer at 1000 K after holding the voltage at 4.8 V for (a) 11 and (b) 267 μs.

NMC as the so-called "partially ordered" pattern, an intermediate between the layered and the rock salt.[2,9,10,40,41] The bright/dark alternation in the Li layer has been interpreted as the "spinel-like" feature from diffraction patterns or fast Fourier transforms of STEM images.[9,12] A comparison of the single-crystal diffraction patterns of different phases will be discussed later. Recently, the bright/dark alternation has also been directly observed in real space with a sharp contrast in STEM images of Li_xNiO_2 held at 4.75 V with respect to Li metal for 2 weeks.[44] In fact, the authors observed both patterns: successive spots with similar intensities in the Li layer near the surface and the bright/dark alternation about 15 nm deeper from the surface, which is consistent with our findings.

Kinetics of the $Li_{0.5}NiO_2$ Spinel Formation. A layered to spinel phase transformation was first observed in Li_xMnO_2.[45−47] However, the kinetics of this transformation are very dependent on the transition metal chemistry,[48] and to our knowledge, no room-temperature bulk transformation of layered to spinel has been observed in Co- or Ni-rich systems. In this section, we show that in the Ni-rich layered compounds conventional spinel formation is too slow to be observed at room temperature. The layered to spinel phase transformation occurs via Ni migration from the transition metal layer to Li layer, with Li shifting from octahedral to tetrahedral sites. In total, 25% of Ni needs to migrate to complete the transition, vacating every other site along both *a* and *b* directions in the transition metal layer. The diffusion path of a single Ni atom has been proposed before.[16,49,50] However, a phase transformation involves many atoms and the interactions between them. We put the energetics of many single-atom migration paths into the training data of the cluster expansion model and try to simulate the complete phase transformation with KMC.

Starting from a half-lithiated layered structure, simulations are run in a 32 × 32 × 4 supercell at various temperatures to study the layered to spinel transformation dynamics. The Ni octahedral occupation in the Li layer, $C(\mathrm{Ni})$, is monitored to calculate the fraction of spinel phase formed, $f_s = C(\mathrm{Ni})/0.25$. Figure 6 shows the evolution of $C(\mathrm{Ni})$ with time at various

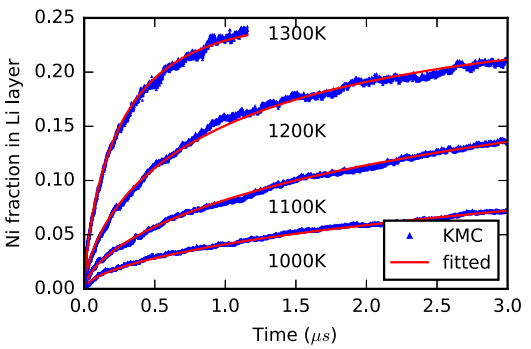

Figure 6. Fraction of Ni in the Li layer as a function of time starting from the half-lithiated layered structure.

temperatures. Owing to the time scale difference between Ni and Li motions, elevated temperatures are required to observe a significant amount of Ni migration. The phase transformation dynamics can be well fitted by the Kolmogorov−Johnson−Mehl−Avrami (KJMA) model[51,52]

$$f_s = 1 - \exp(-(Kt)^n) \quad (1)$$

where t is time, K is the overall rate constant, and n is the Avrami's exponent. The fitted curves at different temperatures are plotted on top of the numerical data in Figure 6, and the

DOI: 10.1021/acsenergylett.9b00122
ACS Energy Lett. 2019, 4, 811−818

fitting results are listed in Table 1. The R^2 of the regressions are all above 0.989, indicating a good match between the model and data. The rate constant K can be extrapolated to lower temperatures using the Arrhenius equation. Figure 7 shows a semilogarithmic plot of the rate against $1/T$. The overall transformation barrier calculated from the slope is 1.57 eV. The n values from the fittings are between 0.58 and 0.72, slightly decreasing as the temperature drops. Extrapolating T to 300 K and taking $n = 0.4$, the half-life of the layered $Li_{0.5}NiO_2$ to spinel transformation is around 6×10^3 h at room temperature. Varying n does not change the order of magnitude of this estimate. This low value of the transformation rate constant is consistent with experimental in situ powder X-ray diffraction studies showing that the layered to spinel transformation for compositions around $Li_{0.5}NiO_2$ is only observed at elevated temperatures, between 450 and 600 K.[16,17,53]

Table 1. KJMA Fit Results

T (K)	n	K (1/μs)	R^2
1000	0.58	0.065	0.989
1100	0.61	0.224	0.995
1200	0.64	0.884	0.997
1300	0.72	3.519	0.996

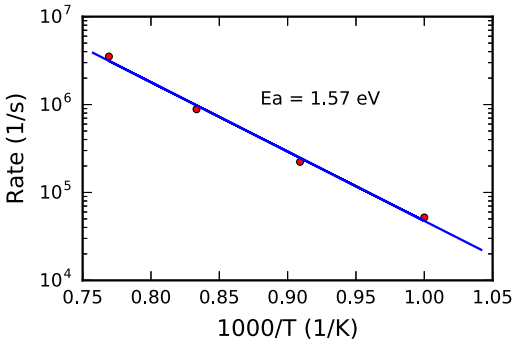

Figure 7. Arrhenius plot of the layered to spinel phase transformation rate. The barrier is 1.57 eV from a linear regression.

The Avrami's exponent n is often related to the phase transformation mechanism in experiments. For example, with a constant three-dimensional growth rate, a zero nucleation rate leads to $n = 3$; a constant nonzero nucleation rate results in $n = 4$; and diffusion control gives $n = 1.5$.[54−56] There is no consensus about the physical meaning of $n < 1$. Nevertheless, n is characteristic of different processes. Interestingly, a n value of 0.65 was also found in an experimental study on the $MgAl_2O_4$ spinel formation from MgO and Al_2O_3 mixtures.[57]

Comparison with Experimental Diffraction Patterns. Experimental selected area electron diffraction (SAED) measurements of the surface densified phases show not only the spinel-like double spacing spots on top of layered features but also spots from certain zone axes that are forbidden for conventional spinel.[12] Previous work was unable to resolve the structure of this surface phase and only referred to it as a "spinel-like" or "defect-spinel" phase. Here we demonstrate that the β and γ phases match all of the diffraction patterns observed. In Figure 8, the single-crystal diffractions of the Ni-excess phases (β, γ, δ) are compared with the perfect layered and the $Li_{0.5}NiO_2$ spinel. Two common zone axes are examined. One is the layered [010] (or equivalently [110]) axis, and the other is the layered $[\bar{1}11]$ axis, which are [110] and [112] in the spinel coordination system, respectively. In the following text, a letter is put in front of the $[uvw]$ vector to show the coordination system used: L for layered and S for spinel. The left-most column in Figure 8 is the spinel reference, and the right-most column is the layered reference. The forbidden spots in the spinel are indicated by red arrows. The β phase has all of the diffraction spots that the spinel has. In addition, the forbidden spots are permitted and have high intensities in β, as indicated by the dashed red circles. The L[010] and L[110] directions are inequivalent in the γ phase but are equivalent in all the other phases. In the γ phase, the diffraction pattern from the L[010] direction is the same as

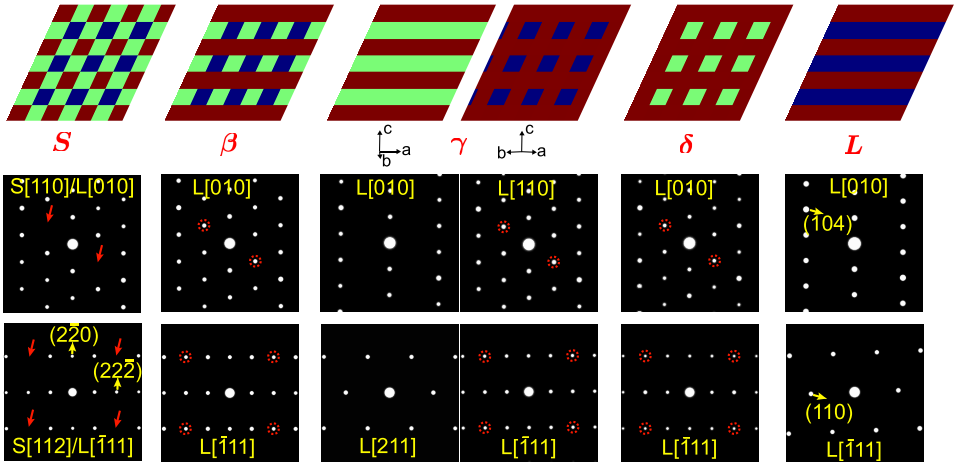

Figure 8. Comparison of Ni column occupancies and single-crystal diffraction patterns of possible phases. The top row shows Ni column occupancies along the L[010]/L[110] axis or the S[110] axis correspondingly. Red is fully occupied, green is half full, and blue is empty. The middle row shows the corresponding single-crystal diffraction patterns of the above images. The bottom row shows the diffractions from a different zone axes, the L$[\bar{1}11]$/L[211] or S[112]. The red arrows indicate the forbidden spots in the spinel phase with the space group $Fd\bar{3}m$, and these spots are emphasized by red circles in the β, γ, and δ phases. The additional double-spacing spots are obvious compared with the diffractions of L.

DOI: 10.1021/acsenergylett.9b00122
ACS Energy Lett. 2019, 4, 811−818

that of the layered and from the L[110] direction is the same as that of the β. Because the diffraction spots from the L[010] direction are a subset of that from the L[110] direction, in a mixture of these two, all of the spinel spots and the forbidden spots will show up but with lower intensities. In the work of Hwang et al., forbidden spots of spinel are clearly shown in the selected area diffraction patterns (SADPs) of surface regions in a cycled NCA sample.[12] Though we did not see much δ phase in the KMC simulations, we put its diffraction here as a reference. The diffraction of the δ phase is similar to that of the β, but the subset of spots corresponding to the rock salt phase are higher in intensity. Combined with the literature data with the KMC simulations, we can confidently claim that the surface phase is not the $Li_{0.5}NiO_2$ spinel but more likely one of the Ni-excess phases, first predicted in the Li−Ni−O phase diagram in ref 19.

The Ni/O ratio is useful to distinguish the Ni-excess phases from the spinel phase in experiments. In our simulations, the Ni content in most parts of the surface densified region does not exceed that of the γ phase, $Ni_{0.5}NiO_2$, i.e., Ni_3O_4. Higher Ni contents appear only after the γ phase grows throughout the entire simulation box, which seldom happens for a particle in a real battery setting. It should also be noted that in reality the presence of the spinel-like phase might not be uniform along the zone axis in a particle as thick as hundreds of nanometers. This means that in the spinel-like region the average Ni/O ratio should be between 1/2 and 3/4. Note that our simulations did not take into account oxygen vacancies whose effects may play a role within a few atomic layers to the surface.

One strategy to suppress the formation of the Ni-excess surface phases is to reduce oxygen loss by coating the surface with a phase that is more resistant to oxygen loss than the fully delithiated layered compound but has suitable Li transport[13,27,58] Several coating materials, such as Li_2ZrO_3 and Al_2O_3, have been used on commercial cathode materials. Spinel phases may however have particular advantages. For a given redox couple, spinels tend to have a higher extraction voltage than layered phases due to the low energy of Li in the tetrahedral site. A spinel phase at the surface would therefore be oxidized only after the bulk is oxidized. Though $Li_{0.5}NiO_2$ spinel cannot easily be formed in bulk form, it should be investigated whether one can direct surface phase transformation toward this phase, potentially by the addition of other spinel-forming elements or by using a synthesis protocol that exploits the fact that spinels usually have low surface energies[59] (and hence may become preferred under certain conditions at the surface). For example, ref 13 successfully synthesized a spinel-coated layered $LiNi_{0.8}Co_{0.1}Mn_{0.1}O_2$ and observed an improvement in cyclability.

In conclusion, the surface phases formed by Ni back diffusion in Ni-rich cathode materials are clarified by atomistic kinetic simulations. The $Li_{0.5}NiO_2$ spinel cannot form from the layered parent phase at room temperature during cycling because of the extremely slow transformation kinetics. Given a surface Ni source, the $Ni_{0.25}NiO_2$ β and $Ni_{0.5}NiO_2$ γ phases emerge near the surface in our KMC simulations. The simulated STEM images and single-crystal diffractions of the above two phases match well with experimental measurements, suggesting that they are more likely structures for the densified phases than spinel or rock salt.

■ ASSOCIATED CONTENT

Supporting Information

The Supporting Information is available free of charge on the ACS Publications website at DOI: 10.1021/acsenergylett.9b00122.

Details of the computational methods (PDF)

■ AUTHOR INFORMATION

Corresponding Author

*E-mail: gceder@berkeley.edu.

ORCID

Penghao Xiao: 0000-0002-5846-6343

Tan Shi: 0000-0003-0312-2639

Present Address

§P.X.: Materials Science Division, Lawrence Livermore National Laboratory, Livermore, California 94550, United States.

Notes

The authors declare no competing financial interest.

■ ACKNOWLEDGMENTS

This work was supported as part of the NorthEast Center for Chemical Energy Storage (NECCES), an Energy Frontier Research Center funded by the U.S. Department of Energy, Office of Science, Basic Energy Sciences under Award #DE-SC0012583. Part of P.X.'s work was performed under the auspices of the U.S. Department of Energy by Lawrence Livermore National Laboratory under Contract Number DE-AC52-07NA27344. We thank Dr. Pinaki Mukherjee and Dr. Hena Das for helpful discussion.

■ REFERENCES

(1) Shikano, M.; Kobayashi, H.; Koike, S.; Sakaebe, H.; Ikenaga, E.; Kobayashi, K.; Tatsumi, K. Investigation of Positive Electrodes after Cycle Testing of High-Power Li-Ion Battery Cells II: An Approach to the Power Fading Mechanism Using Hard X-Ray Photoemission Spectroscopy. *J. Power Sources* **2007**, *174*, 795−799.

(2) Zheng, S.; Huang, R.; Makimura, Y.; Ukyo, Y.; Fisher, C. A. J.; Hirayama, T.; Ikuhara, Y. Microstructural Changes in $LiNi_{0.8}Co_{0.15}Al_{0.05}O_2$ Positive Electrode Material During the First Cycle. *J. Electrochem. Soc.* **2011**, *158*, A357−A362.

(3) Xu, B.; Fell, C. R.; Chi, M.; Meng, Y. S. Identifying Surface Structural Changes in Layered Li-Excess Nickel Manganese Oxides in High Voltage Lithium Ion Batteries: A Joint Experimental and Theoretical Study. *Energy Environ. Sci.* **2011**, *4*, 2223−2233.

(4) Gu, M.; Belharouak, I.; Zheng, J.; Wu, H.; Xiao, J.; Genc, A.; Amine, K.; Thevuthasan, S.; Baer, D. R.; Zhang, J.-G.; Browning, N. D.; Liu, J.; Wang, C. Formation of the Spinel Phase in the Layered Composite Cathode Used in Li-Ion Batteries. *ACS Nano* **2013**, *7*, 760−767.

(5) Boulineau, A.; Simonin, L.; Colin, J.-F.; Bourbon, C.; Patoux, S. First Evidence of Manganese−Nickel Segregation and Densification upon Cycling in Li-Rich Layered Oxides for Lithium Batteries. *Nano Lett.* **2013**, *13*, 3857−3863.

(6) Lin, F.; Markus, I. M.; Nordlund, D.; Weng, T.-C.; Asta, M. D.; Xin, H. L.; Doeff, M. M. Surface Reconstruction and Chemical Evolution of Stoichiometric Layered Cathode Materials for Lithium-ion Batteries. *Nat. Commun.* **2014**, *5*, 3529.

(7) Watanabe, S.; Kinoshita, M.; Hosokawa, T.; Morigaki, K.; Nakura, K. Capacity Fade of $LiAl_yNi_{1-x-y}Co_xO_2$ Cathode for Lithium-Ion Batteries During Accelerated Calendar and Cycle Life Tests (Surface Analysis of $LiAlyNi_{1-x-y}Co_xO_2$ Cathode After Cycle Tests in Restricted Depth of Discharge Ranges). *J. Power Sources* **2014**, *258*, 210−217.

DOI: 10.1021/acsenergylett.9b00122
ACS Energy Lett. 2019, 4, 811−818

(8) Li, J.; Downie, L. E.; Ma, L.; Qiu, W.; Dahn, J. R. Study of the Failure Mechanisms of $LiNi_{0.8}Mn_{0.1}Co_{0.1}O_2$ Cathode Material for Lithium Ion Batteries. *J. Electrochem. Soc.* **2015**, *162*, A1401−A1408.
(9) Sallis, S.; Pereira, N.; Mukherjee, P.; Quackenbush, N. F.; Faenza, N.; Schlueter, C.; Lee, T.-L.; Yang, W. L.; Cosandey, F.; Amatucci, G. G.; Piper, L. F. J. Surface Degradation of $Li_{1-x}Ni_{0.80}Co_{0.15}Al_{0.05}O_2$ Cathodes: Correlating Charge Transfer Impedance with Surface Phase Transformations. *Appl. Phys. Lett.* **2016**, *108*, 263902.
(10) Mukherjee, P.; Faenza, N. V.; Pereira, N.; Ciston, J.; Piper, L. F. J.; Amatucci, G. G.; Cosandey, F. Surface Structural and Chemical Evolution of Layered $LiNi_{0.8}Co_{0.15}Al_{0.05}O_2$ (NCA) Under High Voltage and Elevated Temperature Conditions. *Chem. Mater.* **2018**, *30*, 8431−8445.
(11) Zhang, H.; Karki, K.; Huang, Y.; Whittingham, M. S.; Stach, E. A.; Zhou, G. Atomic Insight into the Layered/Spinel Phase Transformation in Charged $LiNi_{0.80}Co_{0.15}Al_{0.05}O_2$ Cathode Particles. *J. Phys. Chem. C* **2017**, *121*, 1421−1430.
(12) Hwang, S.; Chang, W.; Kim, S. M.; Su, D.; Kim, D. H.; Lee, J. Y.; Chung, K. Y.; Stach, E. A. Investigation of Changes in the Surface Structure of $Li_xNi_{0.8}Co_{0.15}Al_{0.05}O_2$ Cathode Materials Induced by the Initial Charge. *Chem. Mater.* **2014**, *26*, 1084−1092.
(13) Zhang, J.; Yang, Z.; Gao, R.; Gu, L.; Hu, Z.; Liu, X. Suppressing the Structure Deterioration of Ni-Rich $LiNi_{0.8}Co_{0.1}Mn_{0.1}O_2$ through Atom-Scale Interfacial Integration of Self-Forming Hierarchical Spinel Layer with Ni Gradient Concentration. *ACS Appl. Mater. Interfaces* **2017**, *9*, 29794−29803.
(14) Wolverton, C.; Zunger, A. Prediction of Li Intercalation and Battery Voltages in Layered vs. Cubic Li_xCoO_2. *J. Electrochem. Soc.* **1998**, *145*, 2424−2431.
(15) Ceder, G.; Van der Ven, A. Phase Diagrams of Lithium Transition Metal Oxides: Investigations from First Principles. *Electrochim. Acta* **1999**, *45*, 131−150.
(16) Guilmard, M.; Croguennec, L.; Denux, D.; Delmas, C. Thermal Stability of Lithium Nickel Oxide Derivatives. Part I: $Li_xNi_{1.02}O_2$ and $Li_xNi_{0.89}Al_{0.16}O_2$ (x = 0.50 and 0.30). *Chem. Mater.* **2003**, *15*, 4476−4483.
(17) Guilmard, M.; Croguennec, L.; Delmas, C. Thermal Stability of Lithium Nickel Oxide Derivatives. Part II: $LixNi_{0.70}Co_{0.15}Al_{0.15}O_2$ and $Li_xNi_{0.90}Mn_{0.10}O_2$ (x = 0.50 and 0.30). Comparison with $Li_xNi_{1.02}O_2$ and $Li_xNi_{0.89}Al_{0.16}O_2$. *Chem. Mater.* **2003**, *15*, 4484−4493.
(18) Wang, L.; Maxisch, T.; Ceder, G. A First-Principles Approach to Studying the Thermal Stability of Oxide Cathode Materials. *Chem. Mater.* **2007**, *19*, 543−552.
(19) Das, H.; Urban, A.; Huang, W.; Ceder, G. First-Principles Simulation of the (Li−Ni−Vacancy)O Phase Diagram and Its Relevance for the Surface Phases in Ni-Rich Li-Ion Cathode Materials. *Chem. Mater.* **2017**, *29*, 7840−7851.
(20) Liu, W.-W.; Wang, D.; Wang, Z.; Deng, J.; Lau, W.-M.; Zhang, Y. Influence of Magnetic Ordering and Jahn−Teller Distortion on the Lithiation Process of $LiMn_2O_4$. *Phys. Chem. Chem. Phys.* **2017**, *19*, 6481−6486.
(21) Lee, J.; Urban, A.; Li, X.; Su, D.; Hautier, G.; Ceder, G. Unlocking the Potential of Cation-Disordered Oxides for Rechargeable Lithium Batteries. *Science* **2014**, *343*, 519−522.
(22) Urban, A.; Lee, J.; Ceder, G. The Configurational Space of Rocksalt-Type Oxides for High-Capacity Lithium Battery Electrodes. *Adv. Energy Mater.* **2014**, *4*, 1400478.
(23) Urban, A.; Matts, I.; Abdellahi, A.; Ceder, G. Computational Design and Preparation of Cation-Disordered Oxides for High-Energy-Density Li-Ion Batteries. *Adv. Energy Mater.* **2016**, *6*, 1600488.
(24) Peres, J. P.; Delmas, C.; Rougier, A.; Broussely, M.; Perton, F.; Biensan, P.; Willmann, P. The Relationship Between the Composition of Lithium Nickel Oxide and the Loss of Reversibility During the First Cycle. *J. Phys. Chem. Solids* **1996**, *57*, 1057−1060.
(25) Delmas, C.; Peres, J. P.; Rougier, A.; Demourgues, A.; Weill, F.; Chadwick, A.; Broussely, M.; Perton, F.; Biensan, P.; Willmann, P. On the Behavior of The Li_xNiO_2 System: An Electrochemical and Structural Overview. *J. Power Sources* **1997**, *68*, 120−125.
(26) Yoon, C. S.; Jun, D.-W.; Myung, S.-T.; Sun, Y.-K. Structural Stability of $LiNiO_2$ Cycled above 4.2 V. *ACS Energy Lett.* **2017**, *2*, 1150−1155.
(27) Mohanty, D.; Dahlberg, K.; King, D. M.; David, L. A.; Sefat, A. S.; Wood, D. L.; Daniel, C.; Dhar, S.; Mahajan, V.; Lee, M.; Albano, F. Modification of Ni-rich FCG NMC and NCA Cathodes by Atomic Layer Deposition: Preventing Surface Phase Transitions for High-Voltage Lithium-Ion Batteries. *Sci. Rep.* **2016**, *6*, 26532.
(28) Van der Ven, A.; Aydinol, M. K.; Ceder, G.; Kresse, G.; Hafner, J. First-Principles Investigation of Phase Stability in Li_xCoO_2. *Phys. Rev. B: Condens. Matter Mater. Phys.* **1998**, *58*, 2975.
(29) Van der Ven, A.; Aydinol, M. K.; Ceder, G. First-Principles Evidence for Stage Ordering in Li_xCoO_2. *J. Electrochem. Soc.* **1998**, *145*, 2149−2155.
(30) Arroyo y de Dompablo, M. E.; Van der Ven, A.; Ceder, G. First-Principles Calculations of Lithium Ordering and Phase Stability on Li_xNiO_2. *Phys. Rev. B: Condens. Matter Mater. Phys.* **2002**, *66*, No. 064112.
(31) Van der Ven, A.; Ceder, G. Ordering in $Li_x(Ni_{0.5}Mn_{0.5})O_2$ and Its Relation to Charge Capacity and Electrochemical Behavior in Rechargeable Lithium Batteries. *Electrochem. Commun.* **2004**, *6*, 1045−1050.
(32) Wagemaker, M.; Van Der Ven, A.; Morgan, D.; Ceder, G.; Mulder, F. M.; Kearley, G. J. Thermodynamics of Spinel Li_xTiO_2 from First Principles. *Chem. Phys.* **2005**, *317*, 130−136.
(33) Yoon, W.-S.; Iannopollo, S.; Grey, C. P.; Carlier, D.; Gorman, J.; Reed, J.; Ceder, G. Local Structure and Cation Ordering in O3 Lithium Nickel Manganese Oxides with Stoichiometry $Li-[Ni_xMn_{(2-x)/3}Li_{(1-2x)/3}]O_2$ NMR Studies and First Principles Calculations. *Electrochem. Solid-State Lett.* **2004**, *7*, A167−A171.
(34) Hinuma, Y.; Meng, Y. S.; Kang, K.; Ceder, G. Phase Transitions in the $LiNi_{0.5}Mn_{0.5}O_2$ System with Temperature. *Chem. Mater.* **2007**, *19*, 1790−1800.
(35) Malik, R.; Zhou, F.; Ceder, G. Phase Diagram and Electrochemical Properties of Mixed Olivines from First-Principles Calculations. *Phys. Rev. B: Condens. Matter Mater. Phys.* **2009**, *79*, 214201.
(36) Meng, Y. S.; Hinuma, Y.; Ceder, G. An Investigation of the Sodium Patterning in Na_xCoO_2 ($0.5 \leq x \leq 1$) by Density Functional Theory Methods. *J. Chem. Phys.* **2008**, *128*, 104708.
(37) Hinuma, Y.; Meng, Y. S.; Ceder, G. Temperature-Concentration Phase Diagram of P2-Na_xCoO_2 from First-Principles Calculations. *Phys. Rev. B: Condens. Matter Mater. Phys.* **2008**, *77*, 224111.
(38) Wang, Y.; Ding, Y.; Ni, J. Ground-state Phase Diagram of NaxCoO2: Correlation of Na Ordering with CoO_2 Stacking Sequences. *J. Phys.: Condens. Matter* **2009**, *21*, No. 035401.
(39) Bortz, A. B.; Kalos, M. H.; Lebowitz, J. L. A New Algorithm for Monte Carlo Simulation of Ising Spin Systems. *J. Comput. Phys.* **1975**, *17*, 10−18.
(40) Makimura, Y.; Zheng, S.; Ikuhara, Y.; Ukyo, Y. Microstructural Observation of $LiNi_{0.8}Co_{0.15}Al_{0.05}O_2$ after Charge and Discharge by Scanning Transmission Electron Microscopy. *J. Electrochem. Soc.* **2012**, *159*, A1070−A1073.
(41) Kim, N. Y.; Yim, T.; Song, J. H.; Yu, J.-S.; Lee, Z. Microstructural Study on Degradation Mechanism of Layered $LiNi_{0.6}Co_{0.2}Mn_{0.2}O_2$ Cathode Materials by Analytical Transmission Electron Microscopy. *J. Power Sources* **2016**, *307*, 641−648.
(42) Pryor, A.; Ophus, C.; Miao, J. A Streaming Multi-GPU Implementation of Image Simulation Algorithms for Scanning Transmission Electron Microscopy. *Adv. Struct Chem. Imaging* **2017**, *3*, 15.
(43) Ophus, C. A Fast Image Simulation Algorithm for Scanning Transmission Electron Microscopy. *Adv. Struct Chem. Imaging* **2017**, *3*, 13.
(44) Mukherjee, P.; Lu, P.; Das, H.; Faenza, N.; Pereira, N.; Amatucci, G.; Ceder, G.; Cosandey, F. *HAADF STEM Imaging of New Spinel-Like Phases in Ni-Rich Layered Oxide Li-Ion Cathode Materials*;

DOI: 10.1021/acsenergylett.9b00122
ACS Energy Lett. 2019, 4, 811−818

Poster presented at the 19th International Microscopy Congress (IMC19): Sydney, Australia, September 9−14, 2018.
(45) Armstrong, A. R.; Bruce, P. G. Synthesis of Layered $LiMnO_2$ as an Electrode for Rechargeable Lithium Batteries. *Nature* **1996**, *381*, 499.
(46) Capitaine, F.; Gravereau, P.; Delmas, C. A New Variety of $LiMnO_2$ with a Layered Structure. *Solid State Ionics* **1996**, *89*, 197−202.
(47) Vitins, G.; West, K. Lithium Intercalation into Layered $LiMnO_2$. *J. Electrochem. Soc.* **1997**, *144*, 2587−2592.
(48) Reed, J.; Ceder, G. Role of Electronic Structure in The Susceptibility Of Metastable Transition-Metal Oxide Structures to Transformation. *Chem. Rev.* **2004**, *104*, 4513−4534.
(49) Reed, J.; Ceder, G.; Van Der Ven, A. Layered-to-Spinel Phase Transition in Li_xMnO_2. *Electrochem. Solid-State Lett.* **2001**, *4*, A78−A81.
(50) Kim, S.; Ma, X.; Ong, S. P.; Ceder, G. A Comparison of Destabilization Mechanisms of the Layered Na_xMO_2 and Li_xMO_2 Compounds upon Alkali De-Intercalation. *Phys. Chem. Chem. Phys.* **2012**, *14*, 15571−15578.
(51) Avrami, M. Kinetics of Phase Change. I General Theory. *J. Chem. Phys.* **1939**, *7*, 1103−1112.
(52) Avrami, M. Kinetics of Phase Change. II Transformation-Time Relations for Random Distribution of Nuclei. *J. Chem. Phys.* **1940**, *8*, 212−224.
(53) Thomas, M. G. S. R.; David, W. I. F.; Goodenough, J. B.; Groves, P. Synthesis and Structural Characterization of the Normal Spinel $Li[Ni_2]O_4$. *Mater. Res. Bull.* **1985**, *20*, 1137−1146.
(54) Price, C. W. Use of Kolmogorov-Johnson-Mehl-Avrami Kinetics in Recrystallization of Metals and Crystallization of Metallic Glasses. *Acta Metall. Mater.* **1990**, *38*, 727−738.
(55) Málek, J. The Applicability of Johnson-Mehl-Avrami Model in the Thermal Analysis of the Crystallization Kinetics of Glasses. *Thermochim. Acta* **1995**, *267*, 61−73.
(56) Bruna, P.; Crespo, D.; González-Cinca, R.; Pineda, E. On the Validity of Avrami Formalism in Primary Crystallization. *J. Appl. Phys.* **2006**, *100*, No. 054907.
(57) Sinhamahapatra, S.; Shamim, M.; Tripathi, H. S.; Ghosh, A.; Dana, K. Kinetic Modelling of Solid State Magnesium Aluminate Spinel Formation and Its Validation. *Ceram. Int.* **2016**, *42*, 9204−9213.
(58) Aykol, M.; Persson, K. A. Oxidation Protection with Amorphous Surface Oxides: Thermodynamic Insights from Ab Initio Simulations on Aluminum. *ACS Appl. Mater. Interfaces* **2018**, *10*, 3039−3045.
(59) Karim, A.; Fosse, S.; Persson, K. A. Surface Structure and Equilibrium Particle Shape of the $LiMn_2O_4$ Spinel from First-Principles Calculations. *Phys. Rev. B: Condens. Matter Mater. Phys.* **2013**, *87*, No. 075322.

DOI: 10.1021/acsenergylett.9b00122
ACS Energy Lett. 2019, 4, 811−818